

EXAMINING THE POSSIBILITY OF AN ADAF AS THE MAIN POWER
SOURCE BEHIND LINER EMISSIONS

A Thesis
presented to
the Faculty of Natural and Applied Science
at Notre Dame University-Louaize

In Partial Fulfillment of the Requirements for the Degree of
Master of Science
in Astrophysics

by

ELIAS OHANNES DER SAHAGUIAN

December 2019

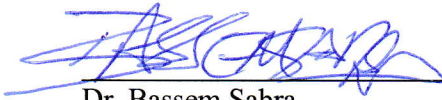
Notre Dame University - Louaize
Faculty of Natural and Applied Science

Department of Physics and Astronomy

We hereby approve the thesis of

Elias Ohannes Der Sahaguan

Candidate for the degree of Master of Science in Astrophysics



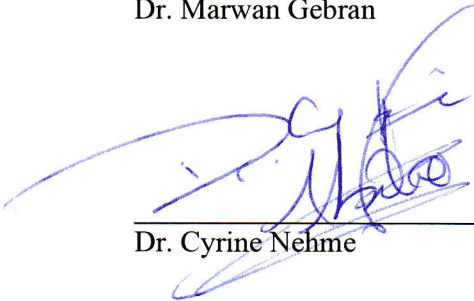
Dr. Bassem Sabra

Supervisor



Dr. Marwan Gebran

Committee Member, Chair



Dr. Cyrine Nehme

Committee Member



Dr. Wehbeh Farah

Committee Member

In loving memory of my father.

Acknowledgements

I thank Dr. Bassem Sabra for his continuous support and mentorship throughout my academic experience and the writing of this dissertation. Without his encouragement and counsel, this research would not have been possible. I would like to thank Dr. Roger Hajar, who played a key role in establishing the Master's of Astrophysics at the Notre Dame University and made this opportunity possible. I also thank Dr. Marwan Gebran and the entire faculty of the Physics Department at FNAS for creating a stimulating academic environment at NDU.

This thesis is written in honor of my late father who always supported my educational pursuits. Lastly, I would like to thank my family and friends, in particular Salman Husain for helping me copy edit this dissertation.

Contents

Acknowledgements	ii
List of Figures	iv
List of Tables	v
Abstract	vi
Résumé	viii
1 Introduction	1
1.1 The Unified Model of AGNs	2
1.2 Excitation Mechanism of LINERs	6
2 Simulations and Data Collection	9
2.1 Photoionization Simulations	9
2.2 The LINER 1.9 Sample	10
2.3 Available UV Spectra for the LINER 1.9 Sample	10
2.4 Available IR Spectra for the LINER 1.9 Sample	12
3 Interpretation of the Diagrams	13
3.1 General Notes	13
3.2 IR Diagrams	15
3.3 Optical-UV Diagrams	21
3.4 UV Diagrams	24
4 Diagrams with Metal Depletion	27
5 Conclusion	36
References	38

List of Figures

1.1	A sketch of the continuum observed for many types of AGNs.	3
1.2	The unified model of Active Galactic Nuclei (AGNs)	5
1.3	An Example of a BPT Diagram)	8
2.1	ADAF SED vs Thin Disk SED	10
3.1	[Ne V] 14.32/[Ne II] 12.81 versus [Ne V] 14.32/[Ne III] 15.55	16
3.2	[Ne V] 14.32/[Ne II] 12.81 versus [Ne III] 15.55/[Ne II] 12.81	17
3.3	[Ne III] 15.55/[Ne II] 12.81 versus [Ne V] 14.32/[Ne III] 15.55	17
3.4	[Ne V] 14.32/[Ne II] 12.81 versus [Ne V] 24.21/[O IV] 25.88	19
3.5	[Ne III] 15.55/[Ne II] 12.81 versus [Ne V] 24.21/[O IV] 25.88	20
3.6	[Ne V] 14.32/[Ne III] 15.55 versus [Ne V] 24.21/[O IV] 25.88	20
3.7	[O III] 5007/ H_{β} versus C IV 1549/He II 1640	23
3.8	[O III] 5007/ H_{β} versus C IV 1549/C III] 1909	23
3.9	C III] 1909]/C II 2326 versus C IV 1549/C III] 1909	24
3.10	C IV 1549/He II 1640 versus C III] 1909/He II 1640	25
3.11	C III] 1909]/He II 1640 versus C IV 1549/C III] 1909	26
3.12	C IV 1549/He II 1640 versus C IV 1549/C III] 1909	26
4.1	[Ne V] 14.32/[Ne II] 12.81 versus [Ne V] 14.32/[Ne III] 15.55 Metal Depleted	28
4.2	[Ne V] 14.32/[Ne II] 12.81 versus [Ne III] 15.55/[Ne II] 12.81 Metal Depleted	29
4.3	[Ne III] 15.55/[Ne II] 12.81 versus [Ne V] 14.32/[Ne III] 15.55 Metal Depleted	29
4.4	[Ne V] 14.32/[Ne II] 12.81 versus [Ne V] 24.21/[O IV] 25.88 Metal Depleted	30
4.5	[Ne III] 15.55/[Ne II] 12.81 versus [Ne V] 24.21/[O IV] 25.88 Metal Depleted	31
4.6	[Ne V] 14.32/[Ne III] 15.55 versus [Ne V] 24.21/[O IV] 25.88 Metal Depleted	31
4.7	[O III] 5007/ H_{β} versus C IV 1549/He II 1640 Metal Depleted	32
4.8	[O III] 5007/ H_{β} versus C IV 1549/C III] 1909 Metal Depleted	33
4.9	C III] 1909]/C II 2326 versus C IV 1549/C III] 1909 Metal Depleted	33
4.10	C IV 1549/He II 1640 versus C III] 1909/He II 1640 Metal Depleted	34
4.11	C III] 1909]/He II 1640 versus C IV 1549/C III] 1909 Metal Depleted	35
4.12	C IV 1549/He II 1640 versus C IV 1549/C III] 1909 Metal Depleted	35

List of Tables

1.1	Criteria for Spectral Classification	6
2.1	Measured and Dereddened Emission-Line Ratios Relative to H_β Provided by Gabel et al 2000[14]	11
2.2	Measured and Dereddened Emission-Line Ratios Relative to H_β Provided by (Dopita et al.[7])	11
2.3	Mid-IR Line Fluxes adopted from (Dudik et al. 2009[9])	12

Abstract

Low-Ionization Nuclear Emission-Line Regions (LINERs) represent the low luminosity end of Active Galactic Nuclei (AGN). The main power source of LINERs is the subject of considerable debate in the scientific community today, despite the fact that some LINERs show features of mass accretion into a super massive black hole (SMBH). Optical line-ratio diagrams are not conclusive diagnostic tools as they can be explained by different mechanisms, including shocks (Dopita et al. 1997[8]) and photoionization accompanied by outflow resembling accretion (Sabra et al. 2003[23]). This dissertation will examine the possibility of an Advection Dominated Accretion Flow (ADAF) as the main power source behind LINER emissions. I focus on a sample of LINER 1.9s that show Narrow Line Region (NLR) emissions with a signature of mass accretion: the broad H_α emission line. The scarcity of available observational data of UV spectra for this sample prompted us to look into IR line-ratios as an additional diagnostic. I compare IR emission line measures adopted from (Dudik et al. 2009[9]) for a set of LINER 1.9s and Optical and UV spectra for NGC 1052 (Dopita et al. 2015[7]) with sets of simulations of a single phase cloud excited by an ADAF source. The models are formed by varying the values of the photoionization parameter and the cloud density using Cloudy (c17.01, Ferland et al 2017[11]). I observe that line-ratios originating from the same element (Carbon and Neon) best fit in an area bounded by column densities ranging between 10^{22} to 10^{23} cm^{-2} and photoionization parameters ranging between $\log(U) = -2.5$ to -2 . Line-ratios involving Carbon versus Helium in the UV or Oxygen versus Neon in the IR are best fit inside these bounded areas,

but only within a dusty metal-depleted model. I note that the $[\text{O III}]5007 / H_{\beta}$ line ratio of NGC 1052 diverge from the best fit scenario by about 1.2 *dex*. Optical and UV observations from a larger set of LINER 1.9s are required to better understand this deviation.

Keywords: AGN - LINER - ADAF - LINE RATIO DIAGNOSIS

Résumé

Les régions de ligne d'émission nucléaire à faible ionisation (LINER) représentent l'extrémité de faible luminosité des noyaux galactiques actifs (AGN). La principale source d'énergie des LINER fait l'objet d'un débat considérable dans la communauté scientifique aujourd'hui bien que certains LINER présentent des caractéristiques d'accrétion de masse dans un trou noir super massif (SMBH). Les diagrammes de rapport de ligne optique ne sont pas des outils de diagnostic concluants car ils peuvent être expliqués par différents mécanismes, y compris les chocs (Dopita et al. 1997[8]) et la photionisation accompagnée d'un écoulement ressemblant à l'accrétion. (Sabra et al. 2003 [23]). Cette thèse examinera la possibilité d'un flux d'accrétion à dominance d'advection (ADAF) comme principale source d'énergie derrière les émissions LINER. Nous nous concentrons sur un échantillon de LINER 1.9 qui montre les émissions de la région de restreinte (NLR) avec une preuve d'accrétion de masse: la large ligne d'émission H_{α} . La rareté des données d'observation disponibles des spectres UV pour cet échantillon nous a incités à examiner les ratios de raies IR comme diagnostic supplémentaire. Nous comparons les mesures des raies d'émission infrarouge adoptées de (Dudik et al. 2009[9]) pour un ensemble de LINER 1.9 et de spectres optiques et UV pour NGC 1052 (Dopita et al. 2015[7]) avec des ensembles de simulations d'un nuage monophasé excité par une source ADAF. Les modèles sont formés en faisant varier les valeurs du paramètre de photoionisation et la densité des nuages en utilisant Cloudy (c17.01, Ferland et al 2017[11]). Nous observons que les ratios linéaires provenant du même élément (carbone et néon) correspondent le mieux à une zone délimitée par des

densités de colonnes comprises entre 10^{22} à 10^{23} cm^{-2} et les paramètres de photo ionisation compris entre $\log(U) = -2,5$ à -2 . Les rapports linéaires impliquant le carbone et l'hélium dans les UV ou l'oxygène et le néon dans l'IR sont les mieux adaptés à l'intérieur de ces zones délimitées, mais uniquement dans un modèle poussiéreux appauvri en métal. Nous notons que le rapport de ligne [O III] 5007 / H_β de NGC 1052 s'écarte du scénario le mieux ajusté d'environ 1,2 dex. Des observations optiques et UV à partir d'un ensemble plus large de LINER 1.9 sont nécessaires pour mieux comprendre cette déviation.

Chapter 1

Introduction

Galaxies with cores that exhibit higher luminosities compared to nearby galactic nuclei, or spectral energy distributions (SED) that cannot be accredited solely to stars, are called Active Galaxies and their compact central sources are called Active Galactic Nuclei (AGN). While it is easy to pinpoint high luminosity AGNs that have a range of luminosities between several orders of magnitude greater than their host galaxies to luminosities that completely outshine their host, the lower spectrum of AGNs is more difficult to identify. Unlike H II regions which are predominantly excited by star formation, AGNs are believed to be powered by mass accretion into a super massive black hole (SMBH). The high luminosity over a range of the electromagnetic spectrum, the emission of strong broad lines like that of H_β and [O III], or the existence of jets are all indicators of excitation through accretion. But as core luminosities decrease and as emission lines from weakly ionized atoms such as [O II] and [N II] become more dominant over strongly ionized atoms such as [He II] and [O III], the excitation mechanism behind such observations becomes more and more vague.

Low-Ionization Nuclear Emission-line Regions (LINERs) that were first defined by (Heckman 1980[16]) show dominance in line emissions of weakly ionized atoms over strongly ionized ones. LINERs show H_α luminosities ranging between 10^{38} and $10^{40} \text{ erg s}^{-1}$, making them more similar to giant H II regions than other AGNs. But the presence of a compact

UV or X-ray core, broad H_α emission lines or radio jets in some LINERs show evidence of some sort of accretion into SMBH; thus LINERs are categorized in the lower luminosity end of AGNs. Despite the fact that a variety of possible excitation mechanisms, ranging from shock waves to hot new stars, were introduced in an attempt to explain the cause of LINER emission, a conclusive scenario was never put forward.

This dissertation will examine the possibility of an Advection Dominated Accretion Flow (ADAF) as an excitation mechanism behind the LINER phenomenon.

1.1 The Unified Model of AGNs

As shown in Figure 1.1, the SED of an AGN is best described by a power law $F_\nu \propto \nu^{-\alpha}$ where α , called the spectral index, is consistent with frequencies in the same spectral band with a typical range of $0.5 \leq \alpha \leq 2$. A common feature of all AGNs is the Big Blue Bump, which is the signature for mass accretion into a super massive black hole. The smaller IR bump is due to thermal processes. It is also clear that AGNs can be classified into two types: radio loud and radio quiet. Over a frequency range between ν_1 and ν_2 the total power $P_{(\nu_1, \nu_2)}$ received is:

$$\begin{aligned} P_{(\nu_1, \nu_2)} &= \int_{\nu_1}^{\nu_2} F_\nu d\nu = \int_{\nu_1}^{\nu_2} C\nu^{-\alpha} d\nu \\ &= \frac{C}{1-\alpha} (\nu_2^{1-\alpha} - \nu_1^{1-\alpha}) \quad (\alpha \neq 1) \\ &= C \ln \left(\frac{\nu_2}{\nu_1} \right) \quad (\alpha = 1) \end{aligned}$$

Even though all AGN SEDs are best fitted by a power law, the different features of AGNs determine their classification into various classes and sub-classes. Such features can in-

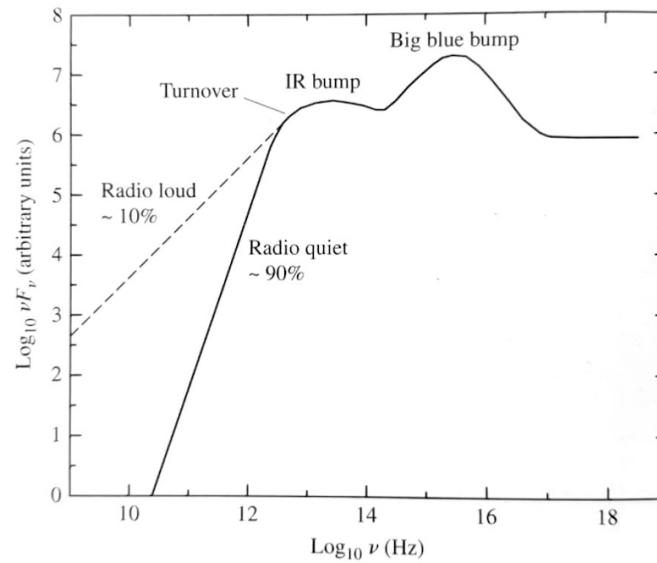


Figure 1.1: A sketch of the continuum observed for many types of AGNs. It is generally believed that the Big Blue Bump is due to accretion disk and the Infrared bump due to thermal processes. (Figure adapted from 'An Introduction to Modern Astrophysics' by B.W.Carroll and D.A.Ostlie)

clude continuum luminosity, variability, radio emission, emission line width and line properties (e.g. allowed/forbidden lines, low/high ionization lines), and the presence of radio lobes or jets. In fact, the idea for a unified model for the AGN phenomena proposed by (Urry and Padovani 1995[27]) was not thought about until recently. The primary reason for this delayed understanding of the unified model is likely due to the fact that two major classes of AGNs were first discovered using different methods.

The first optical spectrum of an AGN was observed at Lick Observatory by Edward E. Fath in 1908 while studying the spiral galaxy NGC 1068. In 1943, Carl Seyfert was the first to report that several resolved galaxies show a stellar appearing core with high surface brightness and unusual emission-line characteristics (Seyfert 1943[24]). This class of active galaxies is now known as Seyfert Galaxies and are sub-classified into two types:

- **Type 1 Seyfert Galaxies** show “narrow-line” emissions in their SEDs that include both allowed and forbidden lines - a characteristic of low-density ionized gas - superposed with “broad-line” emissions lacking forbidden lines - a characteristic of high

density ionized gas.

- **Type 2 Seyfert Galaxies** show only “narrow-lines” in their SEDs and a continuum that is significantly less luminous than Seyfert 1s

Meanwhile in the late 1950s, the first radio sky surveys revealed a more violent celestial object: a quasi-stellar radio source, which became known as a Quasar. When first detected, the star-like compact object displayed broad emission lines, hence the name quasi-stellar radio source. Quasars are now sub-classified as radio-loud and radio-quiet Quasi-stellar Objects (QSOs). QSOs are related to high redshifts and have large UV flux.

The AGN family also includes Radio Galaxies (AGNs that expose large radio fluxes in their core, halo or as forms of jets or lobes), Blazars (AGNs with high variability and high degree of polarization at visible wavelength), Altraluminous Infrared Galaxies (ULIRGs), Low Luminosity AGNs (LLAGNs), and Low Ionization Nuclear Emission-line Regions (LINERs).

Figure 1.2 summarizes the unified model of AGNs: the different classes of AGNs that are observed are not caused by intrinsic physical differences, but rather by the orientation of our line of sight. The central power source of AGNs are obscured by thick circumnuclear matter. A thin disk accretion into a SMBH ionizes its vicinity. A Broad Line Region (BLR) closer to the accretion disk with high velocity and a high density profile is the origin of the broad emission lines. A less dense Narrow Line Region (NLR) is the origin of forbidden narrow emission lines. A more face-on view will allow observers to see emissions from both BLR and NLR, thus classified as type I, and a more edge-on view will obscure emissions from the BLR and show only narrow forbidden lines, thus classified as type II. For a full face-on point of view, Blazars are observed as the observer is looking at jets directed into his point of view.

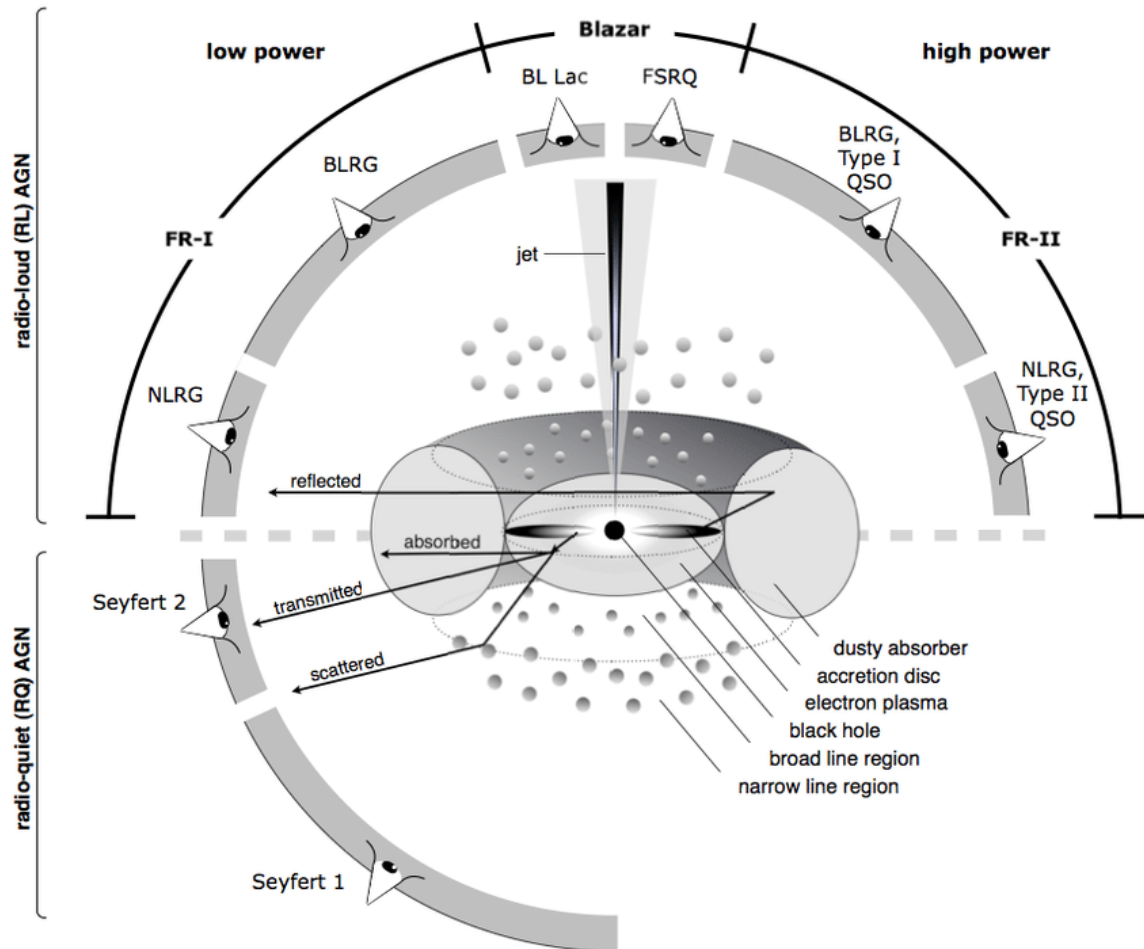


Figure 1.2: The unified model of Active Galactic Nuclei (AGNs). Credit: (Beckmann and Shradar 2012[5]).

1.2 Excitation Mechanism of LINERs

LINERs were first identified by (Heckman 1980[16]) as a class of AGNs that show optical line-emission spectra that broadly resembles that of Seyferts, but are characterized by the strength of line emissions from weakly ionized atoms such as [O II] and [N II], which are weaker in Seyferts. In contrast Seyferts show line emissions from strongly ionized atoms such as [He II] and [O III]. Heckman defined LINERs as nuclei having emission-line flux ratios that satisfy the relations $[O II]\lambda 3727/[O III]\lambda 5007 > 1$ and $[O I]\lambda 6300/[O III]\lambda 5007 > 1/3$.

A more detailed classification was done by (Ho et al. 1997[18]), where galactic nuclei were classified into “pure” LINERs, H II regions and transition nuclei that show line characteristics between LINERs and H II regions. Table 1.1 sums up the criteria of classification proposed by (Ho et al. 1997[18])

Table 1.1: Criteria for Spectral Classification

Class	$[O III]\lambda 5007/H\beta$	$[O I]\lambda 6300/H\alpha$	$[N II]\lambda 6583/H\alpha$	$[S II]\lambda\lambda 6716, 6731/H\alpha$
H II nuclei	Any	< 0.08	< 0.6	< 0.4
Seyfert nuclei	≥ 3	≥ 0.08	≥ 0.6	≥ 0.4
LINERs	< 3	≥ 0.17	≥ 0.6	≥ 0.4
Transition nuclei	< 3	$\geq 0.08, < 0.17$	≥ 0.6	≥ 0.4

Note: Line ratios are dereddened values. $H\alpha$ and $H\beta$ indicate the narrow component of those lines. (Ho et al. 1997[18]).

LINER emissions are very common in galactic nuclei as they make up around 30% of nearby galaxies and the bulk (1/2 – 3/4) of the AGN population (Ho et al. 1997[18]). Most LINERs are of early-type E/S0/Sa galaxies.

The main power source of LINERs is the subject of considerable debate in the scientific community today, despite the fact that some LINERs show features of mass accretion into

a super massive black hole. Other possible power sources include fast shocks (Heckman 1980[16]), photoionization by hot stars (Filippenko & Terlevich 1992[13]; Shields 1992[25]), or photoionization by old, metal-rich stellar populations (Taniguchi et al. 2000[26]).

Advection Dominated Accretion Flow (ADAF) was first introduced by Ichimaru (1977)[19] when he stated that in some accretions the energy dissipated by viscosity can go into heating the matter in the flow rather than being radiated away. After finding the solution for such flows, numerical models were soon established and studies about ADAF characteristics were put forward (Abramowicz et al. 1996[1]) (Narayan et al. 1997[20]). Having sub-Eddington accretion, ADAFs are very radiatively inefficient, geometrically extended, similar in shape to a sphere (or a “corona”) rather than a disc, and very hot (close to the virial temperature). Because of their low efficiency, ADAFs are much less luminous than the Shakura-Sunyaev thin discs. ADAFs emit a power-law, non-thermal radiation, often with a strong Compton component[2].

This dissertation examines the possibility of an ADAF as an excitation mechanism behind the LINER phenomenon by plotting ratios of emission line strength of different atoms gathered from observations and comparing them to ratios calculated by models. These diagrams are called BPT diagrams. These diagrams were first introduced as techniques to probe excitation mechanisms by Baldwin, Phillips and Terlevich in 1981[3], hence their given name.

Figure 1.3 shows an example of a BPT diagram. In a BPT diagram, observational data of line ratios are plotted and analyzed for certain tendencies and to look for clusters of emission regions that have the same type of power source to investigate the properties of those regions. Simulated models can be computed and their results compared to observations as a means of testing the validity of the model.

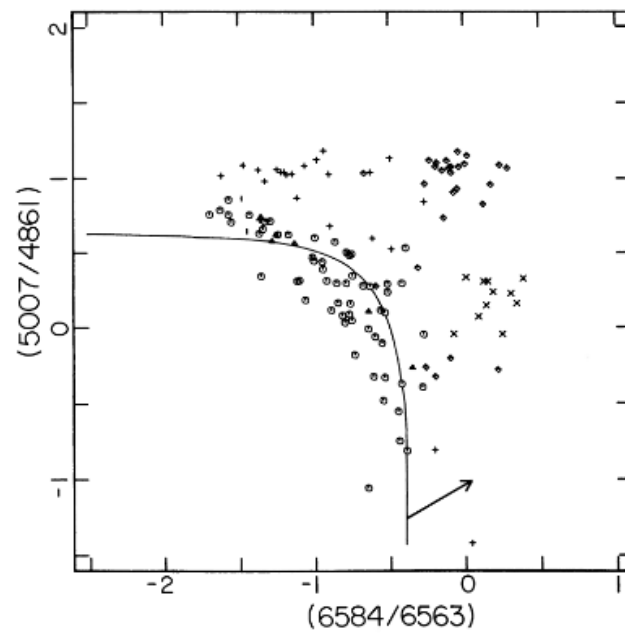


Figure 1.3: An Example of a BPT Diagram[3] For certain emission lines, observations are gathered from different types of objects (e.g. HII regions, AGNs) and their strength ratios are plotted to investigate their general properties.

Chapter 2

Simulations and Data Collection

2.1 Photoionization Simulations

For the simulations, I use Cloudy (c17.01, Ferland et al 2017) to emulate the photoionization caused by an ADAF source on different clouds. Cloudy is a spectral synthesis code designed to simulate conditions in interstellar matter under a broad range of conditions. I choose a cloud with solar abundances, varying its hydrogen column density and the photoionization parameter for each model. Because this study examines extragalactic regions, the hydrogen column density is considered as the measure of the approximate amount of matter in the vicinity of the AGN: more precisely it constrains the size of the cloud near the NLR. The ionization parameter U is defined as the ratio of ionizing photon density to hydrogen density $U = \frac{n_\gamma}{n_H}$ and it constrains the dimensionless intensity of ionizing radiation.

For the Hydrogen column densities, I use five different values of 10^{20} , 10^{21} , 10^{22} , 10^{23} and 10^{24} cm^{-2} and I set up a grid of a photoionization parameter running from -4.0 to $+4.0$ in steps of 0.5 dex to be performed with each Hydrogen column density value. I note that some simulations gave a null value to certain emission lines, so these lines were deducted from the diagrams below.

I use an ADAF SED determined through observation by (Nemmen et al.2014[21]). Figure 2.1 shows the ADAF SED in black compared to a thin disk SED. The main distinction between an ADAF SED to a thin disk one is that it is flatter over a range of frequencies and lacks the Big Blue Bump.

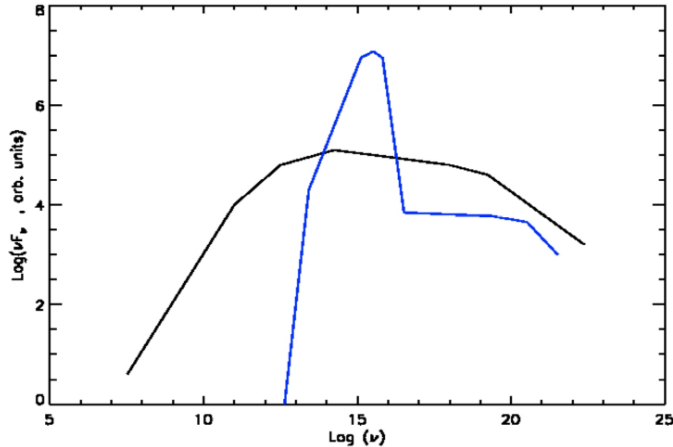


Figure 2.1: The blue line is a thin disk SED and the black line is the ADAF SED taken from (Nemmen et al. 2014[21]). They are normalized at 10 R_{yd}, the vertical scale is arbitrary.

2.2 The LINER 1.9 Sample

To compare the photoionization simulations to observable data, I choose a sample of 22 LINER 1.9s, a sub-class of LINERs that show broad H_{α} lines. The decision to reduce the sample to LINER 1.9s was made to test whether the emission lines can be explained by an ADAF source continuum for LINERs with a signature of black hole powered accretion (the broad H_{α} lines).

2.3 Available UV Spectra for the LINER 1.9 Sample

During my research, I found that the UV spectra available for the LINER 1.9 sample above is outdated and almost all IUE spectra are either not usable for UV spectral line extraction or do not have the required spectral coverage. The only accessible spectra for data retrieval

was an FOS observation done on NGC 1052. (Gabel et al. 2000[14]) performed a detailed analysis of NGC 1052. Table 2.1 shows the results of the flux strength of different UV and Optical lines extracted by (Gabel et al. 2000[14]) after being dereddened.

Table 2.1: Measured and Dereddened Emission-Line Ratios Relative to H_β Provided by Gabel et al 2000[14]

Line	$E(B - V) = 0.02$	$E(B - V) = 0.44$
<i>C IV</i> $\lambda 1549$	0.14(± 0.04)	0.75(± 0.64)
<i>He II</i> $\lambda 1640$	0.16(± 0.05)	0.80(± 0.66)
<i>C III]</i> $\lambda 1909^a$	0.35(± 0.08)	2.00(± 1.73)
<i>C II]</i> $\lambda 2326^b$	0.58(± 0.08)	3.80(± 3.51)
[<i>O II]</i> $\lambda 3727$	2.77(± 0.31)	3.98(± 0.81)
[<i>O III]</i> $\lambda 5007$	2.85(± 0.32)	2.72(± 0.32)
H_β $\lambda 4861$	1 ^c	1 ^d

^a Line deblending procedure required for flux measurement.

^b Contains [*O III* $\lambda 2321$ and *Si II* $\lambda 2335$] emissions.

^c $F_{H_\beta} = 2.65(\pm 0.13) \times 10^{-14} \text{ ergs s}^{-1} \text{ cm}^{-2}$

^d $F_{H_\beta} = 1.1(\pm 0.7) \times 10^{-14} \text{ ergs s}^{-1} \text{ cm}^{-2}$

A more recent observation on NGC 1052 was made using the Wide Field Spectrograph (WiFeS; Dopita et al. 2010[6]) at the ANU 2.3 m telescope at Siding Spring Observatory. This study adopted the data reduction by (Dopita et al. 2015[7]) where nuclear line fluxes were derredened by $A_v = 1.05$. The final extracted line fluxes relative to H_β are shown in Table 2.2.

Table 2.2: Measured and Dereddened Emission-Line Ratios Relative to H_β Provided by (Dopita et al.[7])

$\lambda(A)$	Line ID	Obs. Flux ^a ($H_\beta = 100$)
1548, 51	C IV	72 \pm 12
1640	He II	74 \pm 9
1907, 09	C III]	129 \pm 7
2326, 35	C II] Si II]	107 \pm 13
3726, 29	[O II]	403 \pm 8
5007	[O III]	241 \pm 4

^a Absolute dereddened flux in aperture: $F(H_\beta) = 9.04 \times 10^{14} (\text{erg cm}^{-2} \text{ s}^{-1})$

2.4 Available IR Spectra for the LINER 1.9 Sample

The IR spectroscopic data is adopted from (Dudik et al. 2009[9]), in which a comprehensive mid-infrared spectroscopic investigation was conducted for 67 LINERs using archival observations from the high-resolution modules of the Infrared Spectrograph on board the Spitzer Space Telescope. The following table summarizes the LINER 1.9 data available in that study.

Table 2.3: Mid-IR Line Fluxes adopted from (Dudik et al. 2009[9])

Galaxy Name	[Ne II] 12 μ m	[Ne III] 15 μ m	[Ne V] 14 μ m	[Ne VI] 24 μ m	[O IV] 26 μ m
NGC 1052	21.03 \pm 0.3	12.4 \pm 0.2	0.54 \pm 0.15	2.5 \pm 0.4	2.1 \pm 0.5
NGC 2681	8.5 \pm 0.5	3.4 \pm 0.2	< 0.1	< 0.27	2.3 \pm 0.4
NGC 2787	1.5 \pm 0.1	1.0 \pm 0.1	< 0.03	< 0.12	< 0.3
NGC 3226	2.0 \pm 0.2	1.9 \pm 0.1	< 0.14	< 1.4	< 1.4
NGC 3642	9.8 \pm 0.4	2.3 \pm 0.1	< 0.07	0.90 \pm 0.17	1.2 \pm 0.3
NGC 3884	2.1 \pm 0.1	1.1 \pm 0.1	< 0.04	< 0.11	< 0.1
NGC 3998	12.2 \pm 0.1	7.8 \pm 0.2	< 0.10	< 1.8	< 1.5
NGC 4036	5.1 \pm 0.1	3.0 \pm 0.1	< 0.02	0.90 \pm 0.16	0.9 \pm 0.2
NGC 4143	3.2 \pm 0.1	2.3 \pm 0.1	< 0.04	< 0.15	0.6 \pm 0.2
NGC 4203	1.8 \pm 0.1	2.1 \pm 0.1	< 0.03	< 0.30	< 0.5
NGC 4278	5.6 \pm 0.1	4.0 \pm 0.1	< 0.03	0.70 \pm 0.14	1.6 \pm 0.1
NGC 4438	22.2 \pm 0.8	8.6 \pm 0.5	< 0.21	1.1 \pm 0.19	3.5 \pm 0.5
NGC 4450	3.8 \pm 0.9	2.5 \pm 0.6	< 0.71	< 1.46	1.8 \pm 0.7
NGC 5005	41.8 \pm 0.7	13.3 \pm 0.7	< 0.14	< 0.39	< 0.8

Note: Line fluxes are given in units of $10^{-21} W cm^{-2}$.

3σ upper limits are reported for nondetections. (Dudik et al. 2009[9]).

Chapter 3

Interpretation of the Diagrams

3.1 General Notes

Various inputs affect spectral line strengths, including the ionization parameter, hardness of the radiation source, and the properties of the surrounding cloud (e.g. chemical composition, thickness, geometry and density, to mention a few). The simulations performed in this study examine the effects of the photoionization parameter and cloud density on the spectral line strengths by varying the inputs for each of these two variables only. Other variables, such as chemical composition and cloud geometry, are excluded from the first set of simulations, by selecting, for example, an isotropic single phase cloud with solar metallicity; however, in the analysis of the BPT diagrams that follow, chemical composition is taken into account and proves to be a key factor in adjusting the models in order to meet the observed data. Cloud geometry, on the other hand, may significantly impact line strengths of some elements, like the optical $[OIII] \lambda 5007$ line, but will be only briefly addressed in this dissertation and will be the subject of future examination to improving the models.

Lines originating from higher ionized atoms of the same element generally tend to be strengthened with the increase in the value of the photoionization parameter. This is also clear within the simulations when increasing the photoionization parameter, but a cutoff oc-

curs at $\log(U) = -1$ where all IR lines null down to zero. UV lines undergo a substantial decrease at $\log(U) = -1$ and disappear directly afterwards. A photoionization parameter of a value lower than $\log(U) = -4$ also results in the absence of IR lines. Therefore, for the purpose of having a more expanded picture of the relevant data, the values of $\log(U)$ in the diagrams range between -4 and -1.5 for both IR and UV spectral lines.

In the diagrams bellow, each color represents a cloud with a specific Hydrogen column density, ranging from 10^{20} cm^{-2} (orange) to 10^{24} cm^{-2} (blue). The different photoionization parameter values are represented by the colored circles. The first circle of each colored curve in all the diagrams (always starting on the bottom left) begin with photoionization parameter $\log(U) = -4$, while the successive circles on the same colored path (generally moving diagonally to the upper right) represent a sequence of increasing photoionization parameter by 0.5 dex . For clarity of the positions of the observed line ratios in the diagrams, some of the higher photoionization parameter values are not shown. For the same reason, the first circle on the bottom left of Figure 3.1 represents a photoionization parameter value of $\log(U) = -2.5$

The following sections present an analysis of the BPT diagrams resulting from the previously mentioned simulation data, taking into account the available observational line spectra. First, I analyze emission line diagrams involving the IR lines, then lines involving the optical and UV, and finally ratios involving UV lines only. LINER emission-line ratios that are adopted from (Dudik et al. 2009[9]) measurements are represented by black stars, except for NGC 1052, which is represented by a red star since it is the only LINER which has observational spectral line data in both IR and UV and allows comparison of line ratios in both IR and UV diagrams.

3.2 IR Diagrams

My study is limited by the scarcity of the observed data; therefore, the IR line ratio diagrams involve only two elements: Neon and Oxygen. In my analysis, I can group the diagrams into two parts: one involving only Neon lines and the other involving both Neon and Oxygen. The reason behind this grouping is the fact that line intensities are generally very dependent on element abundances and can be affected by the metallicity of the cloud. Therefore, when examining emission lines originating from the same element within this study, I reduce line strength correspondence to metallicities and depletion.

The first group of diagrams, that are the ones involving only Neon lines, $[Ne II] 12\mu m$, $[Ne III] 15\mu m$ and $[Ne V] 14\mu m$ (Figures 3.1, 3.2 and 3.3), show a strong linear correlation for simulations having the same column density given different values of the photoionization parameter. As the photoionization parameter increases, the line intensity of higher ionized Neon lines increase relative to the lower ionization lines. Furthermore, the set of simulations with different column densities show a compact, almost predictable trend.

For this set of diagrams, the measured line strengths of the lines $[Ne II] 12\mu m$, $[Ne III] 15\mu m$ and $[Ne V] 14\mu m$ of the LINER 1.9 sample fits perfectly between the boundaries of the simulations. The comparison also shows that the observational data lie between the curves corresponding to the column densities of 10^{21} and 10^{23} cm^{-2} and for photoionization parameter ranging between $\log(U) = -2.5$ and $\log(U) = -2$. The segment corresponding to a column density of 10^{22} cm^{-2} and photoionization parameter ranging between $\log(U) = -2.5$ and $\log(U) = -2$ passes through the middle of the scattered observational data. It is important to note that LINERs are often considered as an extension of Seyferts with a lower ionization parameter of about $\log(U) = -3.5$ (Ferland and Netzer 1983[12]), but as shown here, an ADAF ionization source can explain the observed relative

line strength of Neon with ionization parameters equivalent to that of Seyfert 2.

The line ratios corresponding to the result of the simulation with a higher ionization parameter value of $\log(U) = -1$ and column density of 10^{24} cm^{-2} also overlap the bulk of the line ratios of the observed data. But to assign such high values to both column density and ionization parameter is not suggested by any previous study and is probably unlikely to result in a realistic model. The validity of a model with these characteristics can be further investigated by analyzing diagrams with different line ratios

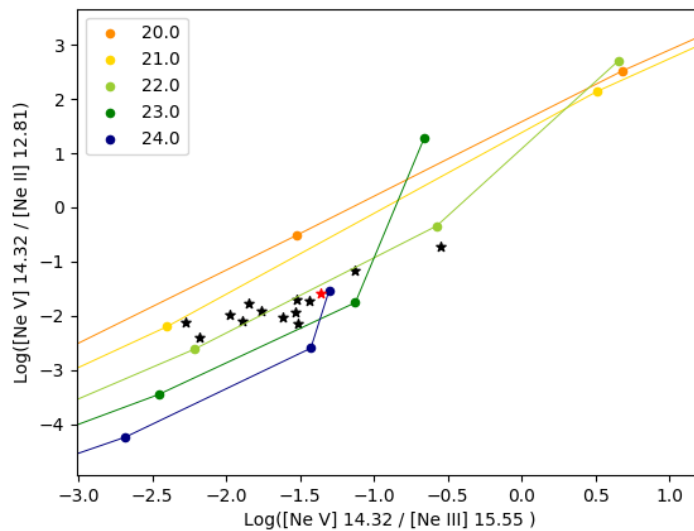


Figure 3.1: $[\text{Ne V}] 14.32/[\text{Ne II}] 12.81$ versus $[\text{Ne V}] 14.32/[\text{Ne III}] 15.55$

Each colored circle represents a Cloudy simulation for a different Hydrogen column density in cm^{-2} (check legend) with photoionization parameter starting from $\log(U) = -2.5$ (bottom left) and increasing in steps of 0.5 dex along the colored curve. The black stars represent the LINER1.9 emission data from Tabel 2.2 except for NGC 1052 represented in red.

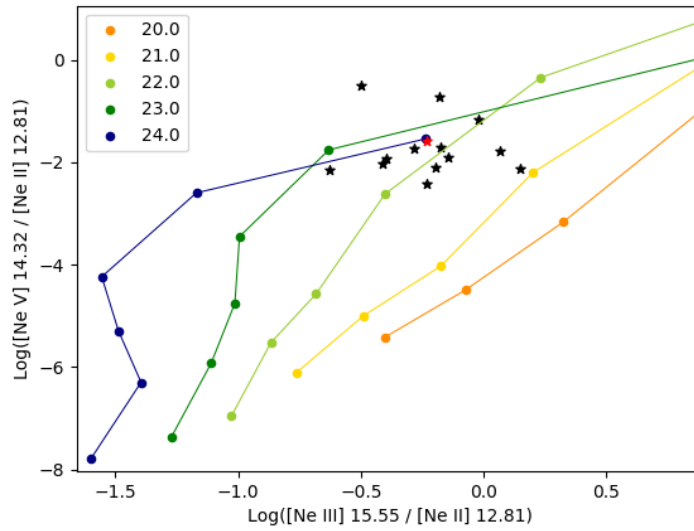


Figure 3.2: $[\text{Ne V}] 14.32/[\text{Ne II}] 12.81$ versus $[\text{Ne III}] 15.55/[\text{Ne II}] 12.81$
 Same as Figure 3.1 with the exception of starting with a photoionization parameter value of $\log(U) = -4$

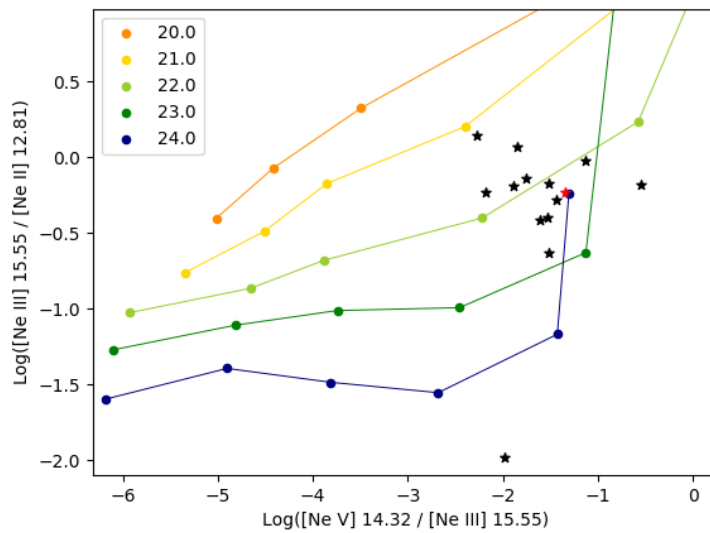


Figure 3.3: $[\text{Ne III}] 15.55/[\text{Ne II}] 12.81$ versus $[\text{Ne V}] 14.32/[\text{Ne III}] 15.55$
 Same as Figure 3.1 with the exception of starting with a photoionization parameter value of $\log(U) = -4$

On the other hand, the second group of diagrams, the ones involving the $[Ne\ VI]\ 24\mu m$ and $[O\ IV]\ 26\mu m$, (Figures 3.4, 3.5 and 3.6), do not show a specific pattern and the results of the simulations with different inputs often closely overlap, especially for moderate photoionization parameter values close to $\log(U) = -2.5$. The results diverge only for higher or lower values. This will make it hard for any observational data to be specified into a certain boundary, thus defining values for photoionization parameter or column density will be more difficult. It is noticeable that there is no clear pattern for the ratio of $[Ne\ VI]\ 24\mu m$ to $[O\ IV]\ 26\mu m$. For column densities 10^{24} and $10^{23}\ cm^{-2}$ the relative strength of $[Ne\ VI]\ 24\mu m$ decreases as the photoionization parameter increases to a threshold where $[O\ IV]\ 26\mu m$ becomes increasing more dominant. This is not the case for the other column densities where the ratios zigzag for different inputs. This shows that the line ratios of different elements might be dependent on many factors and not predominantly dependent on photoionization parameter and column density values.

The predominant feature of this set of diagrams is the over estimation of the $[Ne\ VI]\ 24\mu m$ to $[O\ IV]\ 26\mu m$ ratio by the models. If we consider the results of the BPT diagrams with Neon lines above and take the segment corresponding to a column density of $10^{22}\ cm^{-2}$ and photoionization parameter ranging between $\log(U) = -2.5$ and $\log(U) = -2$ as a possible scenario, we notice that the mean core of the observational data show a lower $[O\ IV]\ 26\mu m$ to $[Ne\ VI]\ 24\mu m$ emission ratio than the predicted simulation by approximately $0.8\ dex$. This result may be due to different factors. One of the factors that was not taken into consideration by this simulation is the depletion of elements due to dust grains. The existence of dust in the narrow line region (NLR) of AGNs was suggested before by (Heckman et al. 1981[17]) and (Ferguson et al. 1997a[10]) and can be a possible explanation for the obtained result. The high extinction found in NGC 1052 $E(B-V)=0.44$ (Gabel et al. 2000[14]) or the relatively lower $E(B-V)=0.33$ (Dopita et al. 2015 [7]) also suggest that a large amount of interstellar gas exists in the nuclear region, which may be due to a

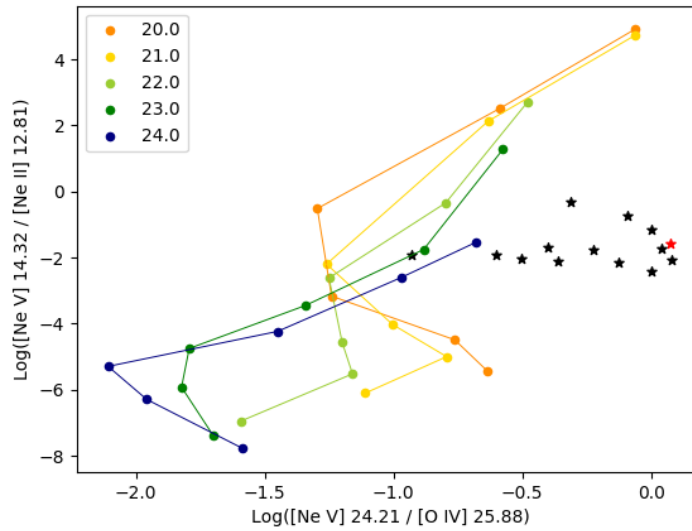


Figure 3.4: $[\text{Ne V}] 14.32/[\text{Ne II}] 12.81$ versus $[\text{Ne V}] 24.21/[\text{O IV}] 25.88$
 Same as Figure 3.1 with the exception of starting with a photoionization parameter value of $\log(U) = -4$

dusty accretion flow. Noble gasses like Neon and Helium are not expected to be effected by such depletion, and thus the relative abundances of such elements may increase in these regions.

It is clear, after a basic analysis of the first IR line ratio diagrams, that constraints on the photoionization parameter strength and cloud density alone are not enough to form a model that can offer a more complete understanding of the medium and power source of line emissions. Simulations should consider other variables including metallicity, depletion and existence of dust grains in order to form a more reliable model to be compared with observations. Thereupon, factors like depletion and grains are introduced into the simulations within this study and the results are discussed in Chapter 4.

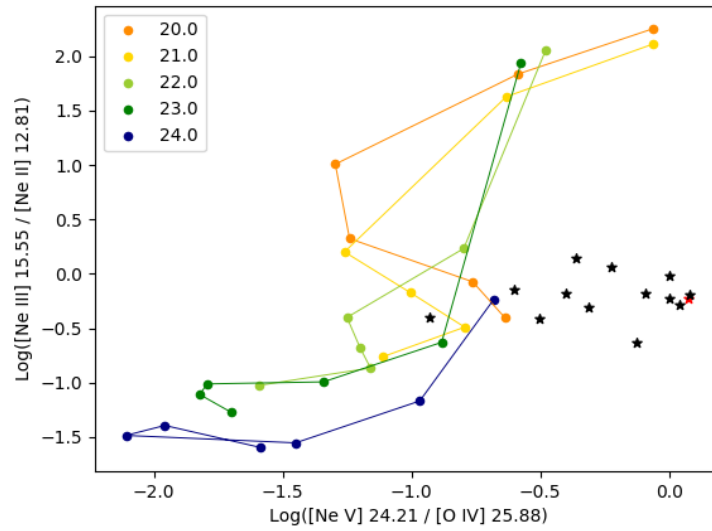


Figure 3.5: $[\text{Ne III}] 15.55/[\text{Ne II}] 12.81$ versus $[\text{Ne V}] 24.21/[\text{O IV}] 25.88$
 Same as Figure 3.1 with the exception of starting with a photoionization parameter value of $\log(U) = -4$

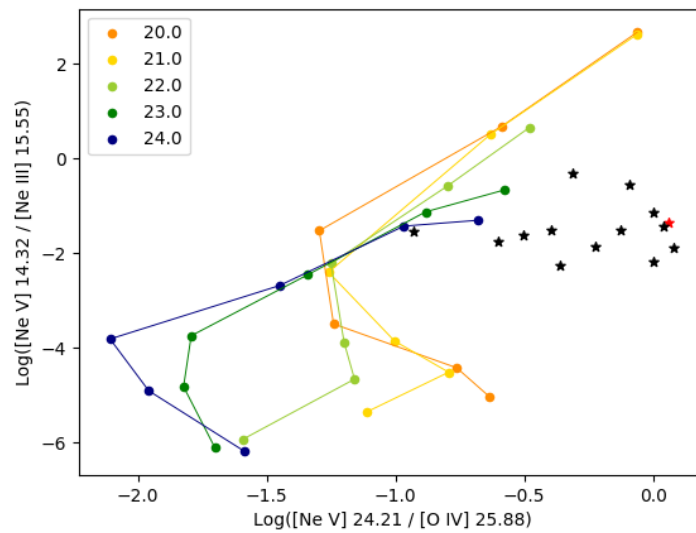


Figure 3.6: $[\text{Ne V}] 14.32/[\text{Ne III}] 15.55$ versus $[\text{Ne V}] 24.21/[\text{O IV}] 25.88$
 Same as Figure 3.1 with the exception of starting with a photoionization parameter value of $\log(U) = -4$

3.3 Optical-UV Diagrams

As mentioned above there is no set of LINER 1.9s with spectral observations over the required range for Optical - UV BPT line diagnostics. Comparing the simulated results to the data available for NGC 1052 can give us an idea about the emission line intensity ratios. However, a conclusive analysis is not possible given the lack of observational data.

Here again, as the photoionization parameter value increases, the strength of the higher ionization lines increase relative to the lower ionization lines. But what is distinguishable is the behavior of the line ratio $[OIII] / H_{\beta}$ for column densities of values 10^{23} cm^{-2} and less, where it is always maximum for $\log(U) = -2$. It is unclear why a photoionization parameter of value $\log(U) = -2$ would maximize the $[OIII]\lambda 5007$ emission, especially because I do not see such a trend emerge for column densities of values above 10^{23} cm^{-2} where the $[OIII] / H_{\beta}$ ratio keeps on increasing with the increase of the photoionization parameter.

If we consider the cloud with column density value of 10^{22} cm^{-2} and photoionization parameter ranging between $\log(U) = -2.5$ and $\log(U) = -2$ as a possible simplification of the NLR of LINER 1.9s, then the ADAF model again fits the ratios that involve emission lines from the same element, in this case $CIV1549/CIII]1909$ (Figure 3.8); however, the model fails to emulate the observed data with regards to two areas: the over estimation of $CIV1549/HeIII1640$ line ratio and the under estimation of the $[OIII] / H_{\beta}$ line ratio.

The case of over estimation, as in the IR line ratios involving Oxygen and Neon, can be explained by the absence of depletion in the simulations. Like Neon, Helium is a Noble gas and is not effected by depletion into dust grains unlike Carbon; therefore, adding depletion to the simulations may also explain the discrepancy.

On the other hand, the case of $[OIII] / H_{\beta}$ optical line ratio underestimation by the model requires a more comprehensive investigation. In attempting to explain the results of the optical line ratios, a comparison with research on NLR of Seyfert II may be insightful. The $[OIII] / H_{\beta}$ line ratios among Seyfert IIs show a variation of about 0.8 dex (Groves and Dopita 2003 [15]). This is still much less than the 2 dex difference between observation and the results of the possible simplified scenario shown in Figure 3.7, but greater than the difference in Figure 3.8 where this deviation drops to about 0.5 dex. I should note here that I am using a single phase cloud model, while all models created in an attempt to explain optical observed line ratios of Seyfert IIs consisted of more than one photoionization component with complex geometries (Nettzer 1990 [22]) (Groves and Dopita 2003 [15]). Another important element in $[OIII]$ line strength is the geometry of the narrow line region. Baskin et al. 2005 [4] shows that the strength of $[OIII]5007$ is mostly modulated by the covering factor of the NLR gas to a greater extent than its density and ionization parameter. The lack of data from different LINER 1.9s also contribute to the problem by making it difficult to look for a pattern among a set of LINER 1.9s or to investigate in any peculiarity in NGC 1052, including the given observation and the correction for reddening. Another, very different suggestion is that the high ionization lines come from the interstellar medium of the host galaxy.(Nettzer 1990 [22])

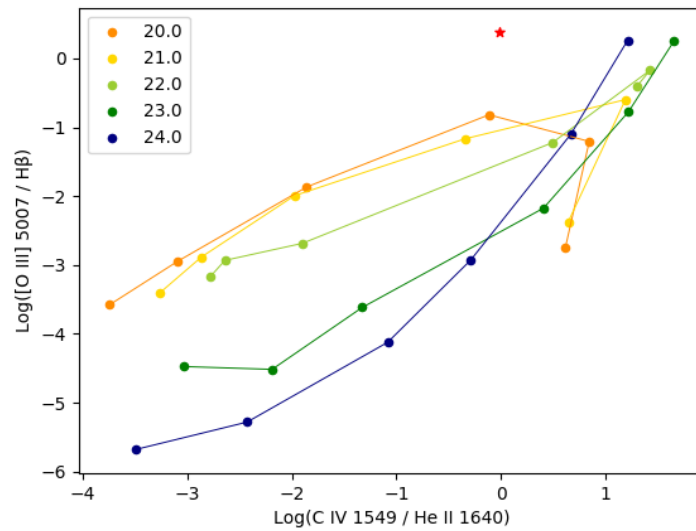


Figure 3.7: $[\text{O III}] 5007/H_{\beta}$ versus $\text{C IV } 1549/\text{He II } 1640$

The colored circles represent the Cloudy simulations for different Hydrogen column density in cm^{-2} (check legend) with photoionization parameter starting from $\log(U) = -4$ (bottom left) and increasing in steps of 0.5 dex along the colored curve. The red star represents the NGC 1052 emission data adopted from Gabel et al.

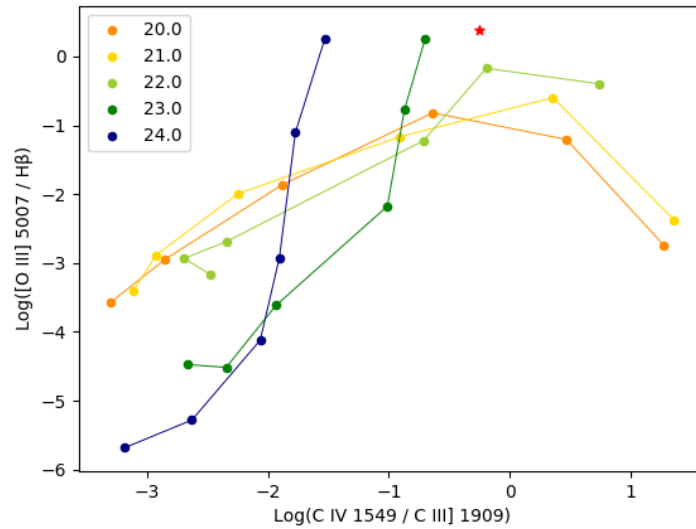


Figure 3.8: $[\text{O III}] 5007/H_{\beta}$ versus $\text{C IV } 1549/\text{C III] } 1909$
Same as Figure 3.7

3.4 UV Diagrams

I treat diagrams involving only UV line ratios the same way as the diagrams involving only IR lines according to two different categories: diagram line ratios from one element only (here Carbon instead of Neon) and diagrams from two different elements (Carbon and Helium instead of Oxygen and Neon).

When dealing with the diagram involving lines emitted from Carbon only that is $CII]2326$, $CIII]1909$ and $CIV]1549$, the position of the NGC 1052 observation data lies in between photoionization parameter values of $\log(U) = -2.5$ and $\log(U) = -2$ for column density of 10^{22} cm^{-2} , reassuring the results of the IR line diagrams. The high ionization $\log(U) = -1$ high density 10^{24} cm^{-2} scenario, which was valid as an explanation in the IR line ratio diagrams, is discarded here since the simulation results do not match with the observed data to a significant degree.

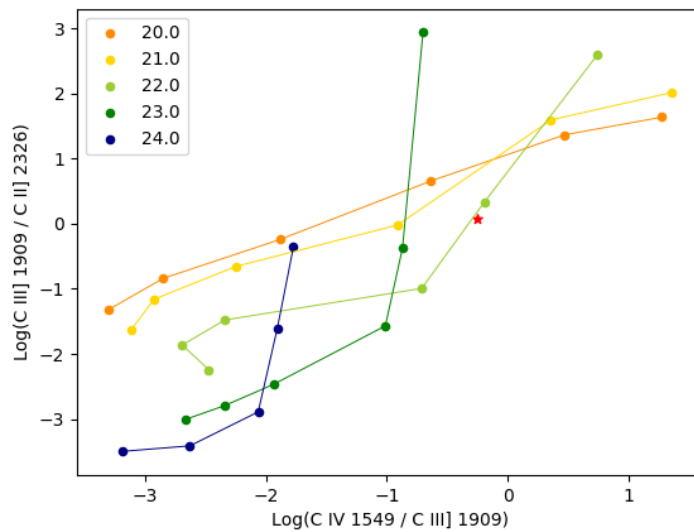


Figure 3.9: $C III] 1909/C II] 2326$ versus $C IV 1549/C III] 1909$
Same as Figure 3.7

The other three diagrams show line ratios with $HeII1640$, $CIII]1909$ and $CIV1549$. It is apparent in the simulations that the line strengths of Carbon lines increase relative to Helium as the photoionization parameter increases; furthermore, a trend similar to the results of the Optical diagrams involving $[OIII] / H_{\beta}$ is also exhibited in the IR diagrams. For column densities that have values of 10^{23} cm^{-2} and lower, the strength of Carbon lines relative to $HeII1640$ is maximized at $\log(U) = -2$, while for denser models the strength of Carbon lines keeps on increasing in accordance with the increase of the photoionization parameter. The models overestimate line ratios of Carbon versus Helium compared to the observations on NGC 1052. Here, values in the diagrams can also be explained by metal depletion. Like Neon, Helium is also a Noble gas and would not be effected by depletion, unlike Carbon.

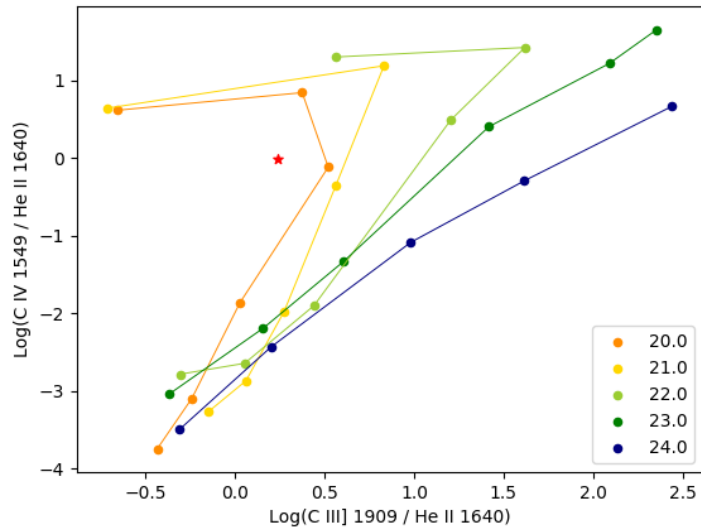


Figure 3.10: C IV 1549/He II 1640 versus C III] 1909/He II 1640
Same as Figure 3.7

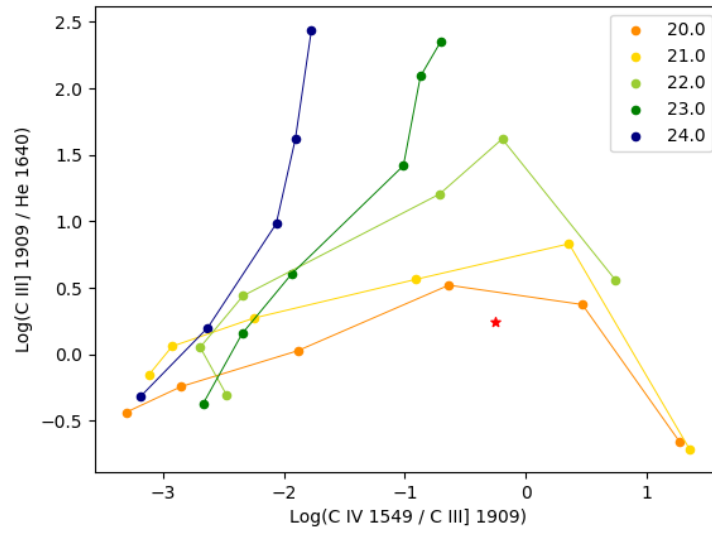
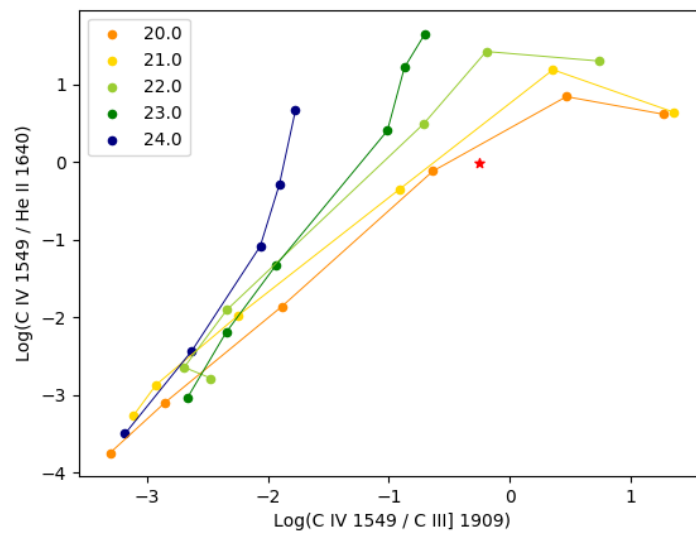


Figure 3.11: C III] 1909/He II 1640 versus C IV 1549/C III] 1909
Same as Figure 3.7



Chapter 4

Diagrams with Metal Depletion

When excluding the diagrams involving the Optical O III emission lines, we notice that the model with a column density of 10^{22} with ionization parameter $\log(U)$ between -2.5 and -2 best fits line ratios originating from the same element; however, it over estimates ratios involving noble gases. The fact that noble gasses are not effected by depletion led me to consider a metal depleted NLR. A metal depleted NLR will also result in the formation of dust grains. As mentioned above, the existence of dust in the NLR of AGNs was suggested before by (Heckman et al. 1981[17], Ferguson et al. 1997a[10]) and the high extinction found in NGC 1052 $E(B-V)=0.44$ (Gabel et al. 2000[14]) or the relatively lower $E(B-V)=0.33$ (Dopita et al. 2015[7]) also suggest a large amount of interstellar gas exists in the nuclear region, which may be due to a dusty accretion flow. Therefore a more consistent simulation should consider a dusty metal depleted cloud.

This chapter re-examines the BPT diagrams above, taking into consideration metal depletion and formation of dust grains. The new simulations use the default depletion suggested by Cloudy (c17.01): in specific, the depletion factor for Carbon and Oxygen are 0.4 and 0.6, respectively. I also add grains to the cloud simulation, because formation of dust grains should be taken into consideration when elements are depleted from the environment. Here also I use the default grains added by Cloudy (c17.01) code.

In the section that follows, I consider each set of diagrams and discuss the major changes in the results of the simulations and the fitting of the observed data.

Figures 4.1, 4.2, 4.3: These diagrams involve Neon IR emission lines. After adding metal depletion and dust grains, the overall line ratio results by the simulations do not change significantly, except that the result of the model with column density $10^{24}/\text{cm}^{-2}$ with $\log(U) = -1$ moves away from the bulk of the observations. The observational data fit an area bounded by column densities ranging between 10^{22} to 10^{23} cm^{-2} and photoionization parameters ranging between $\log(U) = -2.5$ to -2 , which I will describe as the best scenario.

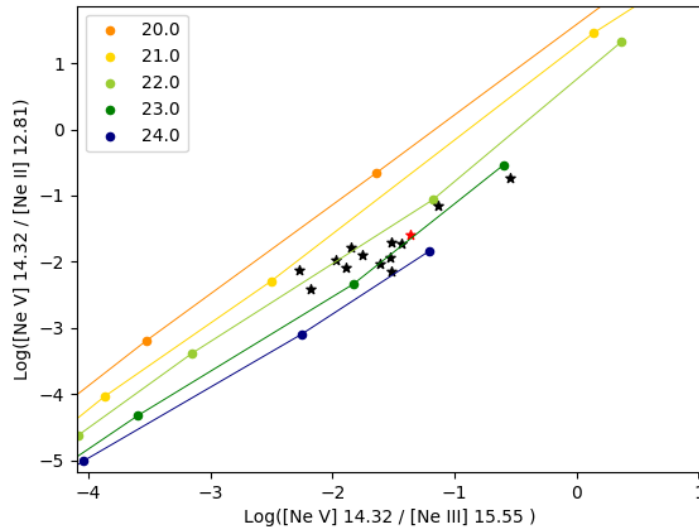


Figure 4.1: $[\text{Ne V}] 14.32/[\text{Ne II}] 12.81$ versus $[\text{Ne V}] 14.32/[\text{Ne III}] 15.55$ Metal Depleted
 Each colored circle represent a Cloudy simulation for a different Hydrogen column density in cm^{-2} (check legend) with photoionization parameter starting from $\log(U) = -2.5$ (bottom left) and increasing in steps of 0.5 dex along the colored curve. The black stars represent the LINER1.9 emission data from Tabel 2.2 except for NGC 1052 represented in red.

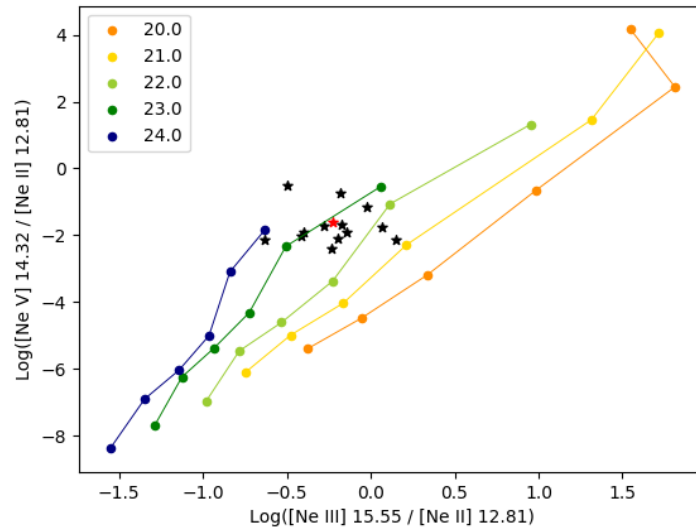


Figure 4.2: $[\text{Ne V}] 14.32/[\text{Ne II}] 12.81$ versus $[\text{Ne III}] 15.55/[\text{Ne II}] 12.81$ Metal Depleted
Same as Figure 4.1 with the exception of starting with a photoionization parameter value
of $\log(U) = -4$

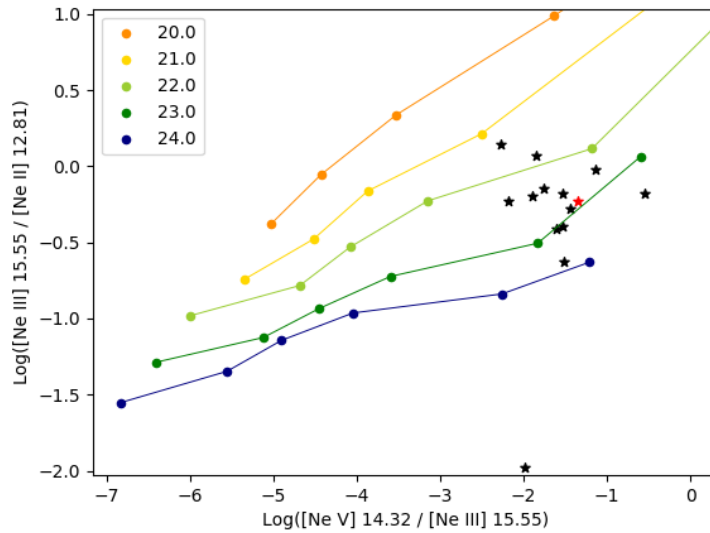


Figure 4.3: $[\text{Ne III}] 15.55/[\text{Ne II}] 12.81$ versus $[\text{Ne V}] 14.32/[\text{Ne III}] 15.55$ Metal Depleted
Same as Figure 4.1 with the exception of starting with a photoionization parameter value
of $\log(U) = -4$

Figures 4.4, 4.5, 4.6: These diagrams involve Neon and Oxygen IR emission lines. After adding metal depletion and dust grains, the overall line ratio results differ by having more of zigzag results rather than steady change in the line ratios as a function of both the photoionization parameters of cloud density. The bulk of the observational results vary by about 0.5 dex from the best fit scenario in contrast of about 1.5 dex in the diagrams without depletion.

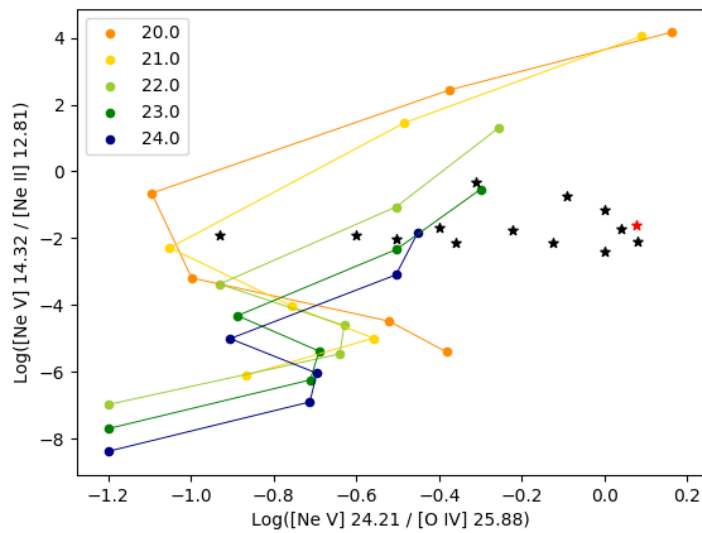


Figure 4.4: $[\text{Ne V}] 14.32/[\text{Ne II}] 12.81$ versus $[\text{Ne V}] 24.21/[\text{O IV}] 25.88$ Metal Depleted
Same as Figure 4.1 with the exception of starting with a photoionization parameter value
of $\log(U) = -4$

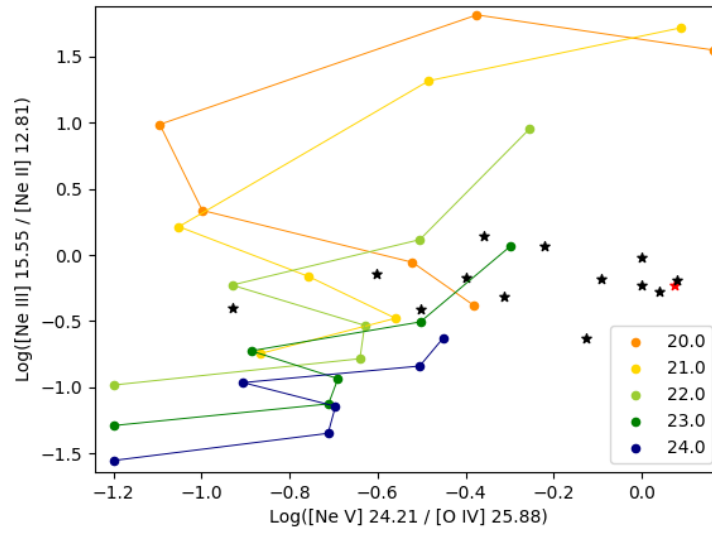


Figure 4.5: $[\text{Ne III}] 15.55/[\text{Ne II}] 12.81$ versus $[\text{Ne V}] 24.21/[\text{O IV}] 25.88$ Metal Depleted
Same as Figure 4.1 with the exception of starting with a photoionization parameter value of $\log(U) = -4$

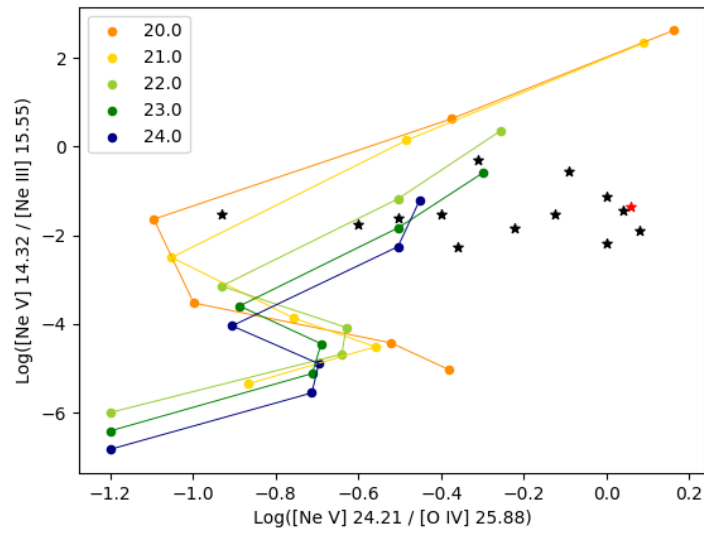


Figure 4.6: $[\text{Ne V}] 14.32/[\text{Ne III}] 15.55$ versus $[\text{Ne V}] 24.21/[\text{O IV}] 25.88$ Metal Depleted
Same as Figure 4.1 with the exception of starting with a photoionization parameter value of $\log(U) = -4$

Figures 4.7, 4.8: These diagrams involve the optical line ratio $[\text{O III}]\lambda 5007/H_\beta$ versus ratios of Carbon and Helium UV emission lines. In contrast to the original diagrams, these two diagrams show a consistency in the discrepancy of the optical $[\text{O III}]\lambda 5007/H_\beta$, where it is underestimated by the model with the best fit scenario by about 1.5 dex. Even though this is a large divergence, the consistency of the variation in both diagrams can be indication that the source of the $[\text{O III}]$ line may be due to an additional emission from the host galaxy.

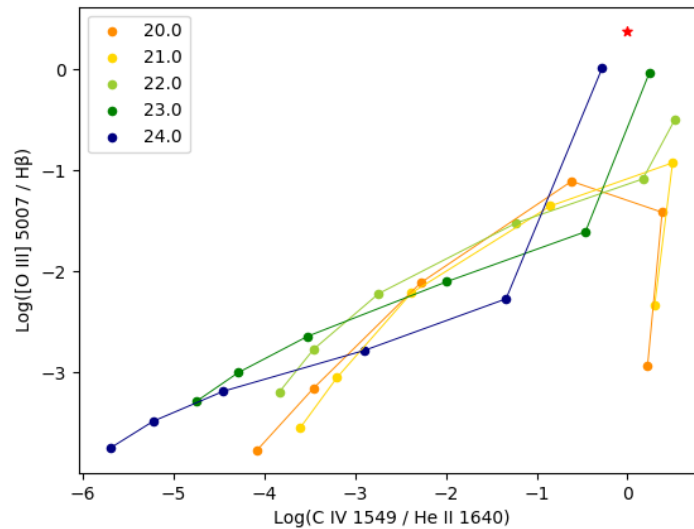


Figure 4.7: $[\text{O III}] 5007/H_\beta$ versus $\text{C IV } 1549/\text{He II } 1640$ Metal Depleted
 The colored circles represent the Cloudy simulations for different Hydrogen column density in cm^{-2} (check legend) with photoionization parameter starting from $\log(U) = -4$ (bottom left) and increasing in steps of 0.5 dex along the colored curve. The red star represents the NGC 1052 emission data adopted from Gabel et al.

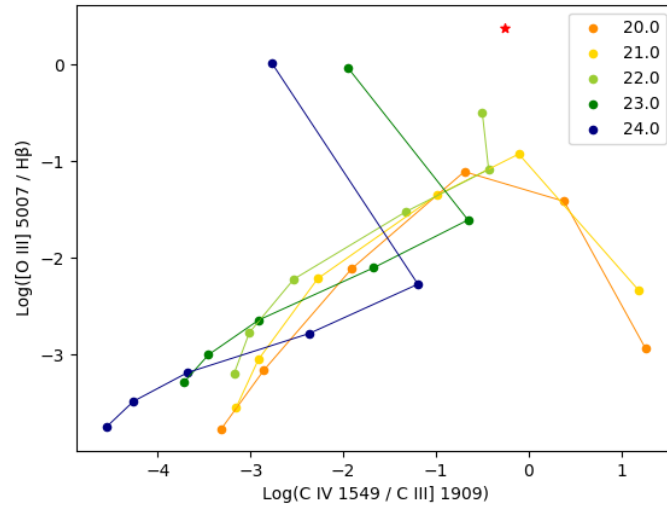


Figure 4.8: $[\text{O III}] 5007/H_{\beta}$ versus $\text{C IV } 1549/\text{C III] } 1909$ Metal Depleted
Same as Figure 4.7

Figures 4.9: This diagram involves the UV Carbon lines only. We notice that the model with the best fit scenario still fits the observational data very well.

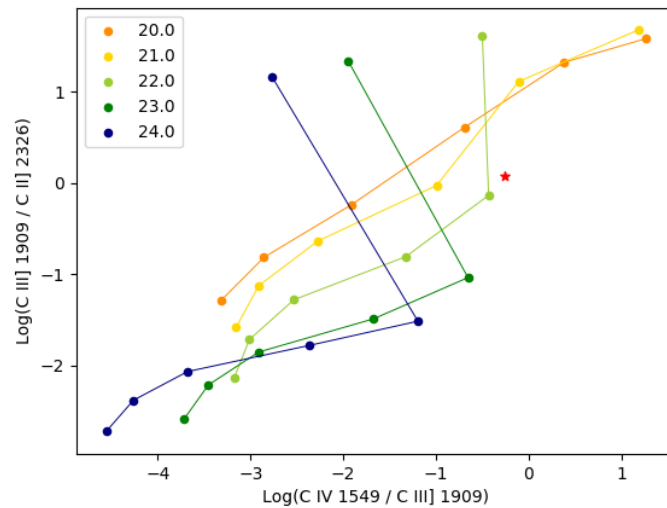


Figure 4.9: $\text{C III] } 1909/\text{C II] } 2326$ versus $\text{C IV } 1549/\text{C III] } 1909$ Metal Depleted
Same as Figure 4.7

Figures 4.10, 4.11, 4.12: These diagrams involve the UV lines emitted from Carbon and Helium. After metal depletion and grains are added, the results of the simulations change as a new pattern emerges. As the photoionization parameter increases, Carbon line strength increases relative to Helium until it reaches $\log(U) = -2.5$, after which the increase in the value of the photoionization parameter intensifies Carbon lines in high density clouds, whereas it intensifies Helium lines in low density clouds. Here again, and after adding metal depletion and dust grains, the model with the best fit scenario meets the observation data of NGC 1052 very well.

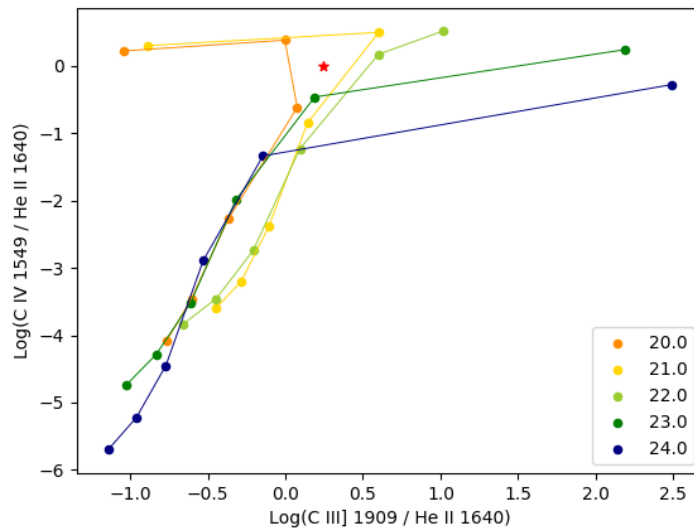


Figure 4.10: C IV 1549/He II 1640 versus C III] 1909/He II 1640 Metal Depleted
Same as Figure 4.7

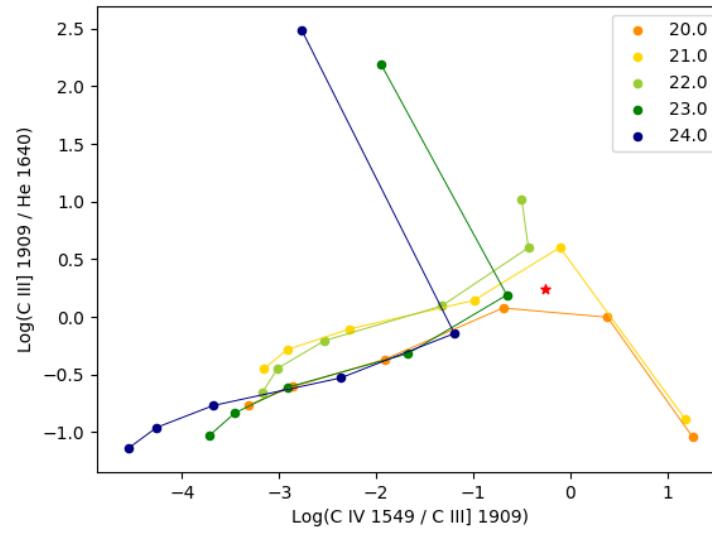


Figure 4.11: C III] 1909]/He II 1640 versus C IV 1549/C III] 1909 Metal Depleted
Same as Figure 4.7

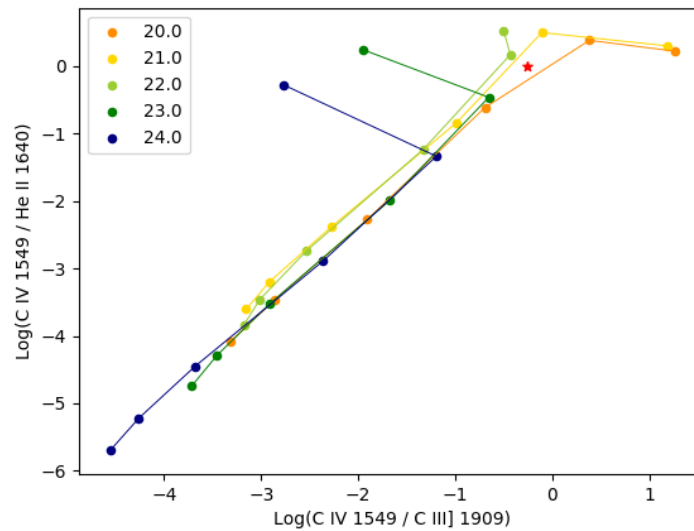


Figure 4.12: C IV 1549/He II 1640 versus C IV 1549/C III] 1909 Metal Depleted
Same as Figure 4.7

Chapter 5

Conclusion

I have compared the ratios of available observation emission line strength in the IR, Optical and UV of a number of LINER 1.9s to simulation models of a single phase cloud excited by an ADAF SED. The results can be summarized as following:

- Emission line ratios from the same element are best described by a model bounded by column densities ranging between 10^{22} to 10^{23} cm^{-2} and photoionization parameters ranging between $\log(U) = -2.5$ to -2 . In contrast to the general belief that LINERs are a lower extension of Seyfert with lower photoionization parameter values, this shows that LINERs may have an equally strong photoionization parameter, but the accretion is better described by an ADAF rather than a thin disk flow.
- This same model also fits observations of ratios involving noble gasses if metal depletion and dust grains are added to the simulation. Thus if we consider a dusty NLR, we will have a more consistent agreement between the updated model and observations.
- The $[\text{O III}]\lambda 5007$ emission line is the only line underestimated by this model. But a dusty NLR model unifies the discrepancy to a 1.2 dex in both Optical diagrams,

which suggests the possibility that the excess $[\text{O III}]\lambda 5007$ might be originating from a different source (for example, star formation), or might be a byproduct of a factor that has not been examined by this dissertation, such as cloud geometry. This disagreement is compared to the line strength observed in NGC 1052 (known to be a star formation region Fernández-Ontiveros et al. 2010), which is the only LINER1.9 with available Optical line data. Thus, more observations are needed in order to investigate this variance.

References

- [1] M. A. Abramowicz, X. M. Chen, M. Granath, and J. P. Lasota. Advection-dominated Accretion Flows around Kerr Black Holes. *1996ApJ*, 471:762, Nov 1996.
- [2] M. A. Abramowicz and O. Straub. Accretion discs. *Scholarpedia*, 9(8):2408, 2014. revision #145813.
- [3] J. A. Baldwin, M. M. Phillips, and R. Terlevich. Classification parameters for the emission-line spectra of extragalactic objects. *1981PASP*, 93:5–19, Feb 1981.
- [4] Alexei Baskin and Ari Laor. What controls the [OIII] λ 5007 line strength in active galactic nuclei? *2005MNRAS*, 358(3):1043–1054, Apr 2005.
- [5] V. Beckmann and C. Shrader. The AGN phenomenon: open issues. In *Proceedings of “An INTEGRAL view of the high-energy sky (the first 10 years)” - 9th INTEGRAL Workshop and celebration of the 10th anniversary of the launch (INTEGRAL 2012). 15-19 October 2012. Bibliotheque Nationale de France*, page 69, Jan 2012.
- [6] Michael Dopita, Jonghwan Rhee, Catherine Farage, Peter McGregor, Gabe Bloxham, Anthony Green, Bill Roberts, Jon Neilson, Greg Wilson, Peter Young, Peter Firth, Gianni Busarello, and Paola Merluzzi. The Wide Field Spectrograph (WiFeS): performance and data reduction. *2010Ap&SS*, 327(2):245–257, Jun 2010.
- [7] Michael A. Dopita, I. Ting Ho, Linda L. Dressel, Ralph Sutherland, Lisa Kewley, Rebecca Davies, Elise Hampton, Prajval Shastri, Preeti Kharb, Jessy Jose, Harish Bhatt, S. Ramya, Julia Scharwächter, Chichuan Jin, Julie Banfield, Ingyin Zaw, Bethan James, Stéphanie Juneau, and Shweta Srivastava. Probing the Physics of Narrow-line Regions in Active Galaxies. III. Accretion and Cocoon Shocks in the LINER NGC 1052. *2015ApJ*, 801(1):42, Mar 2015.
- [8] Michael A. Dopita, Anuradha P. Koratkar, Mark G. Allen, Zlatan I. Tsvetanov, Holland C. Ford, Geoffrey V. Bicknell, and Ralph S. Sutherland. The LINER nucleus of m87: A shock-excited dissipative accretion disk. *The Astrophysical Journal*, 490(1):202–215, nov 1997.
- [9] R. P. Dudik, S. Satyapal, and D. Marcu. A Spitzer Spectroscopic Survey of Low-Ionization Nuclear Emission-Line Regions: Characterization of the Central Source. *2009ApJ*, 691(2):1501–1524, Feb 2009.

- [10] Jason W. Ferguson, Kirk T. Korista, Jack A. Baldwin, and Gary J. Ferland. Locally Optimally Emitting Clouds and the Narrow Emission Lines in Seyfert Galaxies. *1997ApJ*, 487(1):122–141, Sep 1997.
- [11] G. J. Ferland, M. Chatzikos, F. Guzmán, M. L. Lykins, P. A. M. van Hoof, R. J. R. Williams, N. P. Abel, N. R. Badnell, F. P. Keenan, R. L. Porter, and P. C. Stancil. The 2017 Release Cloudy. *2017RMxAA*, 53:385–438, Oct 2017.
- [12] G. J. Ferland and H. Netzer. Are there any shock-heated galaxies ? *1983ApJ*, 264:105–113, Jan 1983.
- [13] Alexei V. Filippenko and Roberto Terlevich. O-Star Photoionization Models of Liners with Weak [O i] λ 6300 Emission. *1992ApJ*, 397:L79, Oct 1992.
- [14] J. R. Gabel, F. C. Bruhweiler, D. M. Crenshaw, S. B. Kraemer, and C. L. Miskey. Hubble Space Telescope Observations and Photoionization Modeling of the LINER Galaxy NGC 1052. *2000ApJ*, 532:883–894, April 2000.
- [15] B. Groves and M. Dopita. *Dust and Radiation Pressure in Narrow Line Regions*, volume 290 of *Astronomical Society of the Pacific Conference Series*, page 207. 2003.
- [16] T. M. Heckman. An optical and radio survey of the nuclei of bright galaxies. Activity in normal galactic nuclei. *1980A&A*, 500:187–199, Jul 1980.
- [17] T. M. Heckman, G. K. Miley, W. J. M. van Breugel, and H. R. Butcher. Emission-line profiles and kinematics of the narrow-line region in Seyfert and radio galaxies. *1981ApJ*, 247:403–418, Jul 1981.
- [18] Luis C. Ho, Alexei V. Filippenko, and Wallace L. W. Sargent. A search for “dwarf” seyfert nuclei. v. demographics of nuclear activity in nearby galaxies. *The Astrophysical Journal*, 487(2):568–578, Oct 1997.
- [19] S. Ichimaru. Bimodal behavior of accretion disks: theory and application to Cygnus X-1 transitions. *1997ApJ*, 214:840–855, Jun 1977.
- [20] Ramesh Narayan, Shoji Kato, and Fumio Honma. Global Structure and Dynamics of Advection-dominated Accretion Flows around Black Holes. *1997ApJ*, 476(1):49–60, Feb 1997.
- [21] Rodrigo S. Nemmen, Thaisa Storchi-Bergmann, and Michael Eracleous. Spectral models for low-luminosity active galactic nuclei in LINERs: the role of advection-dominated accretion and jets. *Monthly Notices of the Royal Astronomical Society*, 438(4):2804–2827, 01 2014.
- [22] H. Netzer. AGN emission lines. In R. D. Blandford, H. Netzer, L. Woltjer, T. J. L. Courvoisier, and M. Mayor, editors, *Active Galactic Nuclei*, pages 57–160, Jan 1990.
- [23] Bassem M. Sabra, Joseph C. Shields, Luis C. Ho, Aaron J. Barth, and Alexei V. Filippenko. Emission and Absorption in the M87 LINER. *2003ApJ*, 584(1):164–175, Feb 2003.

- [24] Carl K. Seyfert. Nuclear Emission in Spiral Nebulae. *1943ApJ*, 97:28, Jan 1943.
- [25] Joseph C. Shields. Normal O Stars in Dense Media Generate LINERs. *1992ApJ*, 399:L27, Nov 1992.
- [26] Yoshiaki Taniguchi, Yasuhiro Shioya, and Takashi Murayama. Poststarburst Models of LINERs. *2000ApJ*, 120(3):1265–1272, Sep 2000.
- [27] C. Megan Urry and Paolo Padovani. Unified Schemes for Radio-Loud Active Galactic Nuclei. *1995PASP*, 107:803, Sep 1995.